Estimating photochemically produced ozone throughout a domain using flight data and a Lagrangian model

J. Methven,[1] S. R. Arnold,[2] F. M. O'Connor,[3] H. Barjat,[4] K. Dewey,[4] J. Kent,[4] and N. Brough[5]

Received 17 September 2002; revised 12 November 2002; accepted 19 December 2002; published 7 May 2003.

[1] Can airborne observations from infrequent flights be used to infer the budget of ozone in the upper troposphere with any degree of certainty or representativeness? Fluctuations in ozone mixing ratio observed along flights are dominated by flying between air masses with distinct origins, rather than the recent chemical transformation that has occurred within those air masses. Reverse domain filling trajectories arriving on a high-resolution three-dimensional grid (RDF3D) can simulate air mass structure accurately by coloring arrival grid points with specific humidity (q) from the origin of each trajectory. Typical displacement errors in tracer filaments are only about 30 km, but the associated phase errors greatly reduce the correlations between airborne observations of long-lived chemicals and their model simulations. However, the comparison can be vastly improved if equivalent potential temperature (θ_e) and specific humidity are used as coordinates to label air masses. Both properties are approximately conserved following unsaturated air and serve as good markers of air masses even if the air is saturated or mixing takes place. Ozone simulations from a Lagrangian model are evaluated against observations in thermodynamic coordinates, factoring out many of the transport phase errors. The proportion of the atmosphere occupied by different chemical air masses is estimated by using RDF3D trajectories to simulate the distributions of q and θ_e and then assuming that chemical composition is homogeneous within air masses, each with characteristic (q, θ_e). Mass density in thermodynamic coordinates is used to weight the modeled ozone transformation and error in concentration (calculated along flight tracks) to estimate photochemically produced ozone throughout a volume encompassing the flights. *INDEX TERMS:* 0325 Atmospheric Composition and Structure: Evolution of the atmosphere; 0365 Atmospheric Composition and Structure: Troposphere—composition and chemistry; 0368 Atmospheric Composition and Structure: Troposphere—constituent transport and chemistry; 3337 Meteorology and Atmospheric Dynamics: Numerical modeling and data assimilation; *KEYWORDS:* air mass averaging, domain filling trajectories, ozone budgets, thermodynamic coordinates

Citation: Methven, J., S. R. Arnold, F. M. O'Connor, H. Barjat, K. Dewey, J. Kent, and N. Brough, Estimating photochemically produced ozone throughout a domain using flight data and a Lagrangian model, *J. Geophys. Res.*, *108*(D9), 4271, doi:10.1029/2002JD002955, 2003.

1. Introduction

[2] The determination of a chemical budget from limited observations is difficult because the path of an air mass has a strong influence on its chemical composition and the path is not known precisely. Emissions and deposition occur predominantly in the boundary layer (BL) and thus the time since air last encountered the BL is important. Above the BL, the chemical composition of the atmosphere depends upon the relative timescales for photochemistry, mixing, and transport by large-scale winds.

[3] The expression "chemical air mass" will be used here to describe a set of trajectories with neighboring origins and distinct chemical characteristics (following *Methven et al.* [2001]). We will also make use of the fact that such air masses tend to have a distinct thermodynamic history too (as discussed by *Bethan et al.* [1998]). A "trajectory" describes the path of a (massless) particle carried by the winds resolved in atmospheric analyses, here from the European Centre for Medium-Range Weather Forecasts (ECMWF). The view taken is that a volume of air centered on a particle trajectory describes an element of an air mass. Unresolved air motions, including convection and three-dimensional

[1]Department of Meteorology, University of Reading, Reading, UK.
[2]School of the Environment, University of Leeds, Leeds, UK.
[3]Department of Chemistry, University of Cambridge, Cambridge, UK.
[4]Met Research Flight, Farnborough, UK.
[5]School of Environmental Sciences, University of East Anglia, Norwich, UK.

0148-0227/03/2002JD002955$09.00

(3-D) turbulence, contribute to sub grid-scale tracer fluxes across its surface, and therefore it is not a material volume. However, the boundary of an air mass described by the envelope of a set of trajectories will follow the resolved flow and stretch under the influence of large-scale strain.

[4] Several timescales are relevant to the transport problem. Large-scale winds stir the atmosphere bringing air masses with distant origins and chemical composition into close proximity. A suitable measure for stirring rate is the Lagrangian decorrelation timescale for horizontal velocity, τ_L [*Ngan and Shepherd*, 1999]. *Methven et al.* [1999] found τ_L to be 0.92 ± 0.06 days on the basis of a 15-year data set of 5 day back trajectories arriving daily at 900 hPa over northwest Europe. Stretching and folding of air masses by the large-scale strain results in sloping tracer sheets which resemble long, thin filaments on a horizontal surface and layers in a vertical profile. Such filaments and layers have been examined in the stratosphere [e.g., *Orsolini et al.*, 1995] and in tropospheric constituents [e.g., *Newell et al.*, 1996]. The formation of layers is often associated with frontogenesis within extratropical cyclones (e.g., the tropopause fold in Figures 1 and 2). During stretching, the width of filaments, and the layer depths, decrease rapidly with time until a scale is reached where mixing is important. The average stretching timescale, τ_s, also varies with location and season [*Pierrehumbert and Yang*, 1993], but an estimate based on finite time Lyapunov exponents, for the northwest European set of trajectories, is 3.3 ± 0.6 days [*Methven et al.*, 1999]. The fact that $\tau_s > \tau_L$ means that contours of a locally released tracer will tend to align rapidly with long-lived background tracers [*Haynes and Anglade*, 1997].

[5] Mixing is very inhomogeneous in the atmosphere and occurs through a variety of processes (e.g., convection, breaking gravity waves) leading to 3-D turbulence and ultimately molecular diffusion, bringing molecules from different air masses into chemical contact. The time taken for an air mass to loose its identity is called the ''mix-down timescale'', τ_m [*Thuburn and Tan*, 1997]. This depends upon the scale at which the air mass characteristics are initially set (e.g., a regional pollution source), the stretching timescale and the scale at which mixing becomes important. It would be difficult to estimate a mix-down timescale in the troposphere due to the inhomogeneity in mixing, however polluted air masses are frequently observed to be distinct for at least a week after leaving the BL [e.g., *Stohl and Trickl*, 1999].

[6] In situations where $\tau_m > \tau_s > \tau_L$, narrow air masses form with almost homogeneous composition but very tight gradients at their edges. If the composition of two air masses is very different, some chemical reactions could occur only at the interface between them. Examples include chlorine activation at the edge of the Antarctic stratospheric polar vortex [*Prather and Jaffe*, 1990; *Edouard et al.*, 1996; *Tan et al.*, 1998] and OH chemistry near the tropopause [*Esler et al.*, 2001]. However, signatures of special interfacial chemistry were not observed in the case discussed in this paper and thus all significant chemistry is assumed to occur within air masses (since the volume of the interfacial regions is very small).

[7] The photochemical timescale for ozone is also long in the free troposphere (e.g., *Roelofs and Lelieveld* [1997] estimate 30 days in summer and 50 days in winter) so that the composition within air masses evolves slowly. However, it is the chemical transformation within air masses and mixing between them, once brought into contact by long-range transport, which determines the evolution of the chemical background state on seasonal timescales and longer. Owing to the difficulty of inferring air mass history and problems of the representativeness of limited observations in the long-term picture, our understanding of such long-term variations is heavily dependent upon models of chemical transport and transformation. Here an analysis technique is described which aims to combine observations and model results in the quantification of domain average chemical transformation and its uncertainty.

[8] The results of the technique will be demonstrated for a single flight of the Met Office C-130 aircraft, collecting chemical data as part of the Atmospheric Chemistry and Transport of Ozone (ACTO) project funded by the Natural Environment Research Council (NERC). The ACTO flight campaign was based in Prestwick, Scotland, during May 2000. In section 2 reverse domain filling trajectories are used to reveal the complex 3-D structure of air masses intercepted by the aircraft. Simulations of specific humidity and θ_e are evaluated directly using the airborne measurements.

[9] Observations of chemical concentration are projected into thermodynamic coordinates (given by observed q, θ_e) in section 3. It is illustrated how most of the variation in ozone can be described by movement of the aircraft between air masses and the average concentration at each point in these 2-D coordinates, providing a great simplification of the 3-D air mass structure evolving over the duration of the flight.

[10] The evolution of air masses is then viewed in thermodynamic coordinates (section 4) illustrating the physical processes affecting them. The average behavior of trajectories (e.g., ascent or descent) at different locations in these diagrams provides a natural means to classify air masses. It is shown how these air mass classes are associated with distinct composition. Additionally, simulations of chemical transformation are projected into these coordinates, providing estimates of the average chemical behavior within each air mass class and estimates of model uncertainty.

[11] The final stage (section 5) is to calculate mass density in thermodynamic coordinates and integrate the chemical transformation, weighted by mass, over each air mass class. The result is the net ozone production that has occurred within the air that occupies the domain encompassing the flight track.

2. Modeling the Structure of Air Masses

2.1. Observations During ACTO

[12] The Meteorological Research Flight (MRF) C-130 aircraft (funded by the Met Office, NERC and DERA) was equipped by the MRF with its regular instruments for ozone, carbon monoxide (CO) and meteorological measurements. Many additional chemical measurements were made, but the only one discussed in this paper is the concentration of reactive odd nitrogen (NO_y) using the University of East Anglia NO_{xy} instrument.

[13] Temperature was measured using a platinum resistance thermometer (Rosemount 102AL) with accuracy ±0.3 K [*Inverarity*, 1999]. Humidity was measured by two instruments: one used Lyman-α fluorescence (mixing ratio accu-

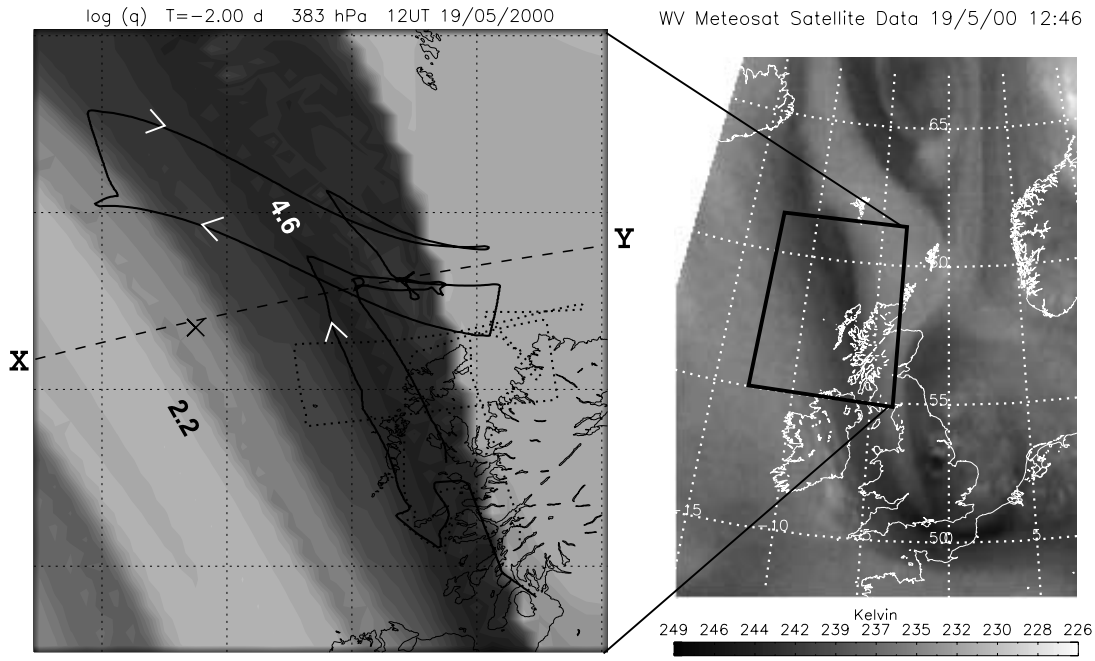

Figure 1. The right panel shows Meteosat water vapor channel brightness temperature at 12:46 UT, 19 May 2000. Blue shading indicates a dry intrusion. The left panel shows a RDF3D simulation of specific humidity at 12 UT, zooming in on the flight domain. Indigo shading is for $\log(q) < -4.6$; orange shading for $\log(q) > -2.2$. The bold dotted line is the aircraft flight track, and the bold solid line is the same track shifted to be relative to the air at 12 UT. The arrows show the direction of flight. The dashed line XY marks the great circle section in Figure 2. See color version of this figure at back of this issue.

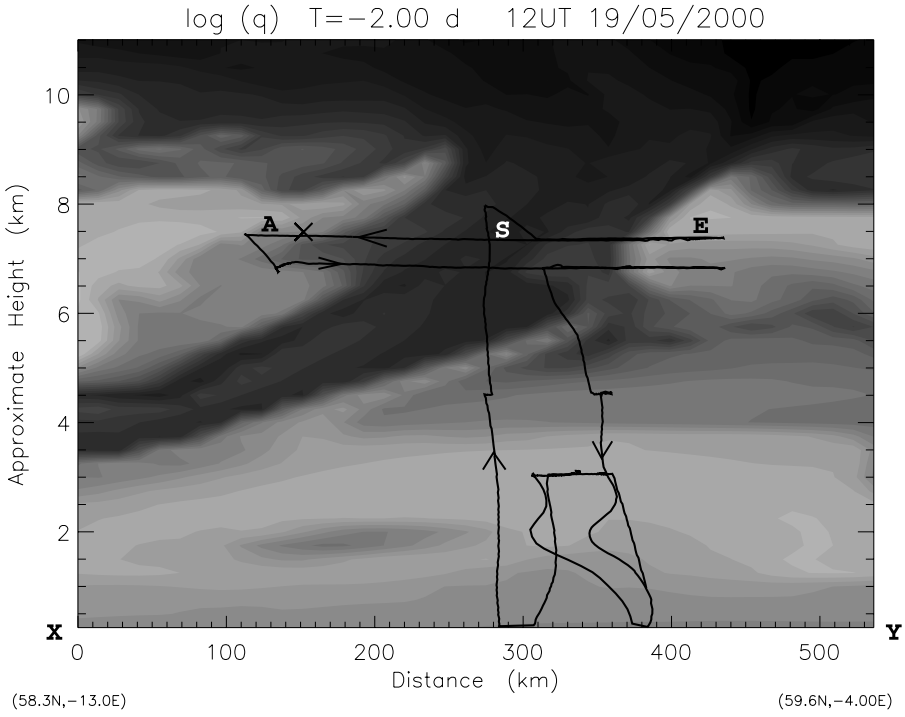

Figure 2. A vertical section across the tropopause fold, seen sloping down to the west. Shading shows specific humidity, as in Figure 1. The solid line shows the projection of the air mass relative flight track onto the section. A, S and E label air masses from the West Atlantic, stratosphere and European boundary layer respectively. See color version of this figure at back of this issue.

racy ±0.015 g kg^{-1}) [*Nicholls et al.*, 1990] and the second was a thermoelectric hygrometer (General Eastern 1011B) measuring dew point temperature (±0.3 K at 270 K; ±1 K at 200 K). The hygrometer has a slow response and lower accuracy at low dew points and so the Lyman-α measurements are shown here in cold, dry air ($q < 0.7$ g kg^{-1}) and the hygrometer measurements elsewhere. The empirical formula of *Bolton* [1980] is used to calculate specific humidity from dew point temperature.

[14] Ozone was measured by a UV absorption technique (Thermo Environmental Instruments Inc., model 49) with accuracy ±3% and the CO instrument used vacuum UV resonance fluorescence (±15% in this experiment) [*Gerbig et al.*, 1999]. NO_y was detected by converting all NO_y species to NO in a gold tube, which was then measured by a chemiluminescence detector (±8 pptv) [*Brough*, 2000].

[15] All instruments have a time resolution of one second or better and the data is stored at the British Atmospheric Data Centre (BADC) at 1s intervals (except NO_y which is averaged over 10s windows). In this paper, all data is averaged over 10s intervals for comparison with the model simulations.

2.2. Lagrangian Model Description

[16] The Lagrangian model used in this paper has two components: the first calculates trajectories following the flow resolved in atmospheric analyses and the second models the evolution of chemical constituents along those trajectories.

[17] The back trajectories are calculated by the U.K. Universities Global Atmospheric Modelling Programme (UGAMP) offline trajectory model [*Methven*, 1997] by integrating velocity with respect to time. The term 'offline' indicates that the dynamical equations of the atmosphere are not integrated as part of the trajectory model. Fields (e.g., velocity, temperature, humidity) at particle positions are obtained from the ECMWF operational analyses by cubic Lagrange interpolation in the vertical followed by bilinear interpolation in the horizontal and linear interpolation in time. The details are given by *Methven* [1997] together with measurements of the errors in trajectories arising from the interpolation of discretized wind fields.

[18] The Cambridge Tropospheric Trajectory model of Chemistry and Transport (CiTTyCAT) simulates chemical transformation following trajectories with a reasonably detailed photochemistry scheme including degradation of some hydrocarbons, a representation of the spread of surface emissions into the boundary layer (using emission inventories) and dry deposition (see *Wild et al.* [1996] and *Evans et al.* [2000] for details). The chemical initial conditions are defined by interpolation of concentration field snapshots, from a full integration of the University of Cambridge global 3-D chemical transport model TOMCAT [*Law et al.*, 1998], in time and space to the origin of each trajectory. TOMCAT was driven using ECMWF analyses at 6 hour intervals from January 1 to May 21, 2000. CiTTyCAT uses pressure, temperature and q interpolated from the ECMWF analyses to the current air mass location.

[19] A more detailed description of the operation of CiTTyCAT with the UGAMP trajectory model is given by *Methven et al.* [2001]. The model operation for this paper is identical, aside from the chemical initialization.

2.3. Reverse Domain Filling Trajectories Revealing 3-D Structure

[20] The flights during the ACTO campaign period (May 2000) were targeted at regions where trajectory model forecasts indicated neighboring air masses with distinct origins. Flight legs were conducted across and along filaments (the appearance of sloping air masses on pressure surfaces). Legs in the across-filament direction were conducted in order to sample a wide variety of air masses and to intercept the target air masses. Once intercepted, the aircraft was steered in the forecast "along-filament direction" for at least 15 minutes, enabling the slower measurement techniques to take a number of samples.

[21] The forecasts of air mass structure were based on Reverse Domain Filling trajectories for a 3-D domain (RDF3D). A high density grid was defined covering the anticipated flight area from the ground to just above the tropopause. Back trajectories were calculated from every point on the 3-D grid from a reference time (t_R; usually 12 UT) near the anticipated flight time. For each RDF3D forecast (made when the latest analysis was available for time t_A) trajectories were integrated backwards in time for three days, using a combination of ECMWF forecasts (if $t - t_A > 0$) or analyses if available ($t - t_A < 0$). Specific humidity was interpolated from the ECMWF forecasts/analyses to the origin of each trajectory (at time interval T before arrival on the grid). These values, $q(t_R - T)$, were used to color the arrival points on the grid, resulting in the RDF3D simulation of air mass structure. Similar results were also obtained using potential vorticity (PV) and θ_e.

[22] The trajectory model was driven by ECMWF forecasts/analyses smoothed to spectral truncation T106 on 60 model levels (defined in a terrain following pressure-based coordinate). *Methven and Hoskins* [1999] have shown that tracer filaments can be simulated accurately with widths at least 6 times smaller than the resolution of the wind field used for trajectory calculation (about 30 km in this case, given analyses every 6 hours). Similarly, the displacement error on the arrival grid in the across-filament direction was expected to be less than 30 km. For this reason, the spacing of the trajectory arrival grid was about 16 km in the horizontal (0.25° in longitude, 0.15° in latitude) and 0.25 km in pressure-height defined by the empirical formula used for air traffic flight levels ($z' = 44330.77[1 - (p/p_o)^{0.19026}]$ m where $p_o = 1013.25$ hPa).

[23] The last flight of the ACTO campaign (19 May 2000) featured a tropopause fold sloping down to the west under the jetstream which was oriented with strong flow (≈45 ms^{-1}) from Iceland towards Scotland. The right panel of Figure 1 shows the Meteosat water vapor channel image for 12:46 UT. The tropopause fold stands out because it is an intrusion of dry stratospheric air. This channel is attenuated strongly by water vapor so that where the atmosphere is anomalously dry, the satellite sees emissions from a lower altitude where the temperature is higher (examples given by *Appenzeller et al.* [1996]). High brightness temperature is shown by blue shading in the image. The box outlines the domain used for the RDF3D simulation of q, shown on the left for trajectory length $T = 2$ days. The correspondence between the humidity simulation and the satellite image is striking.

[24] Back trajectories from neighboring points in the arrival domain separate exponentially with time on average.

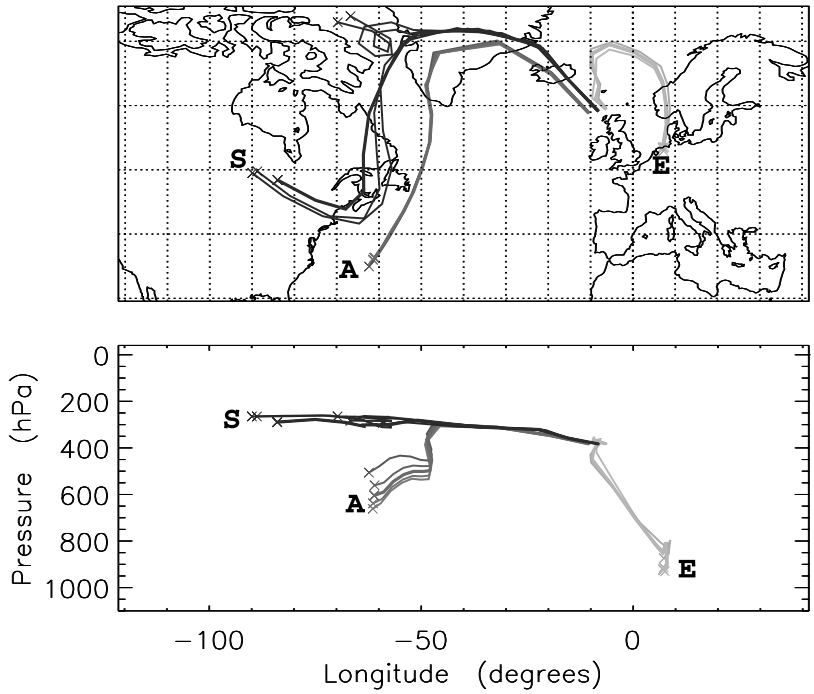

Figure 3. Three day back trajectories from grid points nearest to A, S and E on Figure 2. Lower panel shows pressure along trajectories as they approach the arrival grid.

Trajectories which originate from a region with similar q one day beforehand may separate rapidly as trajectory length, T, is increased until they are diagnosed as coming from regions with different q. This behavior is particularly pronounced if one trajectory experiences ascent and condensation while the other does not. As T is increased, more of the trajectories separate and finer scales are simulated in the arrival domain. Eventually filaments become too narrow to resolve on the RDF3D arrival grid and fall between grid points. For the ACTO period two day trajectories produced fine-scale features which could be just resolved on the chosen arrival grid (although the stepping seen along the eastern edge of the dry intrusion shows how the strip of high q gradient was too narrow to be resolved) and longer trajectories resulted in noisy RDF3D simulations. Throughout the paper two day trajectories are used to simulate thermodynamic variables because they are used to relate the airborne observations to the 3-D air mass structures. However, the CiTTyCAT chemical model is run along 5 day trajectories because photochemical changes in ozone are so slow and the trajectories must also extend into the boundary layer to pick up emissions of ozone precursors.

[25] The flight track of the Met Office C-130 aircraft is shown by the bold dotted line in the RDF3D panel. However, the air masses were moving rapidly, covering great distances over the duration of the flight (almost 5 hours), so that this flight track does not depict the position of the aircraft relative to air masses at the instant t_R. Short forward or back trajectories have been used to shift the flight track with the winds to the reference time t_R, producing an "air mass relative flight track" shown by the bold solid line in Figure 1. Note the strength of the horizontal wind shear across the tropopause fold. The aircraft reached its westernmost point at about 14:30 UT and the shift of this point of the track to the northwest by about 380 km indicates the distance travelled by air in the jetstream over the previous 2.5 hours. The wind was much weaker on the eastern side of the fold.

[26] Figure 2 shows the flight track relative to the position of air masses projected on to cross-section XY (marked on Figure 1) through the fold. The aircraft ascended from the marine boundary layer across the fold, moving north, and dropped to the first flight level at point S, within the stratospheric air. It then turned east out of the fold into air mass E, flew in the along-filament direction within E before heading west directly across the fold into air mass A. The aircraft descended to a lower level, flew along A and then returned across the fold into E. Finally it turned back into the fold and descended below it to the marine boundary layer.

[27] The trajectories arriving at grid points closest to A, S and E on the highest flight leg are shown in Figure 3. Seven trajectories are shown in each set; one in the center, four at the surrounding grid points at that level, one above and one below. Set of trajectories S shows the path of air ending in the stratospheric intrusion. They descended slowly from 250 hPa to 380 hPa over three days. Set A ascended from low levels off the East Coast of the USA and then travelled next to the stratospheric intrusion over the final 1.5 days. Set E ascended steadily over 3 days from the European boundary layer, carrying pollution into the upper troposphere.

2.4. Is the Fine-Scale Structure Real?

[28] The correspondence between the RDF3D simulation of specific humidity and the Meteosat water vapor channel image in Figure 1 indicates that there is value in the simulation on quite fine scales. The satellite would see the deepest part of the dry intrusion as being at its "neck" (where the tropopause is not folded); $d \approx 330$ km on Figure 2. In Figure 1, q is shown on 383 hPa which coincides with the highest flight leg. This surface passes through the

folded part of the intrusion and low q is therefore displaced slightly to the west of the neck seen by Meteosat. Careful comparison of the figures shows the driest q to be within 50 km of the corresponding feature on the satellite image.

[29] The trajectory simulation can be evaluated quantitatively by comparing it with humidity and temperature measured by the aircraft. The bold lines in Figures 4a and 4b show the observed time series of pressure and specific humidity. The two flight levels across the fold are clearly seen at 392 hPa (13:26–14:26 UT) and 428 hPa (14:28–15:28 UT). An extremely sharp gradient in q was observed on the eastern edge of the dry intrusion (between air masses S and E) and a more gradual gradient on the western side in the jetstream (between S and A).

[30] Back trajectories were calculated at regular 10s intervals from the flight track. The pressure at the origin of each trajectory at 12 UT, 17 May 2000 is shown by the dotted line in Figure 4a. Air mass E clearly ascended from 800 hPa to 400 hPa over the last two days. The stratospheric air S descended and air mass A experienced ascent then descent over the period resulting in weak net ascent (compare three day trajectories in Figure 3). Note that the along-flight trajectories are not of equal durations (T) because they arrive on the flight track at different times.

[31] The dotted line in Figure 4b is obtained by interpolating the ECMWF q analysis for 12 UT, 17 May 2000 to the location of each back trajectory at that time. The analyzed value of q in the stratospheric intrusion matches the observed extremely well, especially on the upper flight level. In the air masses that ascended over the period, the analyzed q at trajectory origins is much higher than observed, indicating that condensation has occurred during saturated ascent.

[32] Comparison between potential temperature at trajectory origins (dotted) and the observed value (bold line) in Figure 4c indicates a strong increase over 2 days following air mass E associated with latent heat release from the condensation. The story is confirmed by examining equivalent potential temperature, θ_e, which is conserved following unsaturated or saturated air masses in the absence of external heat sources or mixing. Figure 4d shows clearly that the observed θ_e matches the analyzed value at trajectory origins to within a few Kelvin in air mass E.

[33] In summary, trajectories can model the origin of air masses to the extent that the thermodynamic history of the trajectories is consistent with the values of humidity and temperature observed independently by the aircraft. The fine-scale structures of air masses have been simulated well, although there are timing errors related to displacement errors of the air masses. For example, the tight humidity gradient between S and E is displaced to the east in the simulation (Figure 4b). Section 3.2 presents a method which almost eliminates the effects of such displacement errors.

3. Summarizing Observations and Model Results Within Air Masses

3.1. Averaging in Thermodynamic Coordinates

[34] Since almost all of the variations in thermodynamic properties along the flight track can be described by crossing between air masses with different origins, and those origins may also have distinct chemical characteristics, concentrations are expected to be highly correlated with thermodynamic variables. *Bethan et al.* [1998] and *Cooper et al.* [2001] have used temperature and humidity aircraft data to identify coherent air masses such as warm conveyor belts and dry intrusions and then to estimate the average composition of those air masses. *Parrish et al.* [2000] have used θ_e to color points on scatter plots with ozone and CO as the axes. In this way the characteristic ratios between these longer lived chemical species can be associated with different air masses, identified by their θ_e. Mixing between two air masses can be identified with points clustering along straight lines in these conserved variable diagrams. *Esler et al.* [2003] show clear evidence for mixing between air masses that have been brought together in frontal zones.

[35] Conserved variable diagrams also appear in the literature on moist convection. *Emanuel* [1994] shows examples where total water mixing ratio, r_T, and θ_e define coordinates. Since r_T and θ_e are conserved for reversible, adiabatic processes (including liquid and solid water), an air mass cannot change its location on the diagram without external heating, moisture fluxes from the ground or mixing between air masses. Observations lying along straight lines on the diagram indicate mixing between air masses; for example, mixing between a cumulus updraft carrying properties similar to those at cloud base and its environment.

[36] Unfortunately, it is not possible to construct $r_T - \theta_e$ diagrams here because the liquid and solid water mixing ratios are not given in operational atmospheric analyses. Instead, specific humidity (water vapor) is used which is conserved by adiabatic processes in unsaturated air but can readily be lost by condensation in ascending, saturated air. Pseudo-equivalent potential temperature is used to define θ_e as it only depends upon three variables $\theta_e(\theta, p, q)$ (using the empirical formula of *Bolton* [1980]). This quantity is conserved following pseudo-adiabatic processes where latent heating of air and water vapor is accounted for but the heat capacity of condensate is neglected [see *Emanuel*, 1994]. At saturation $q = q_s(\theta, p)$ reducing the system to two independent variables. At a reference pressure $p_0 = 1000$ hPa, θ_e and q_s depend on only one independent variable, temperature. The curve on the right of both panels in Figure 5 depicts the dependence of θ_e on q as temperature is varied for a saturated air parcel at 1000 hPa.

[37] The distinct thermodynamic properties of air masses enable a reduction in the dimensions needed to describe the data. For example, Figure 5 shows ozone concentration averaged in $\log(q) - \theta_e$ coordinates. The aircraft location in the diagram is obtained by noting the observed values of q and θ_e at regular times along the flight. At each time, t_i, the observed concentration of ozone is used to weight a "kernel" which has a small radius, R, and is centered on the aircraft location in the diagram. The weighted sum of the kernels at each point in thermodynamic coordinates gives the "air mass average". The letters S, A and E label the stratospheric intrusion, American and European air masses as before. The letter B labels the marine boundary layer. Note how the air masses are distinct in these coordinates.

[38] A suitable smooth shape for each kernel is given by:

$$K_i(\mathbf{x}) = \frac{2}{\pi R^2}\left(1 - \frac{r^2}{R^2}\right) \quad (1)$$

for $r < R$, or zero otherwise. In this expression the vector $\mathbf{x} = (x, y)$ denotes any point on the diagram with coordinates $x =$

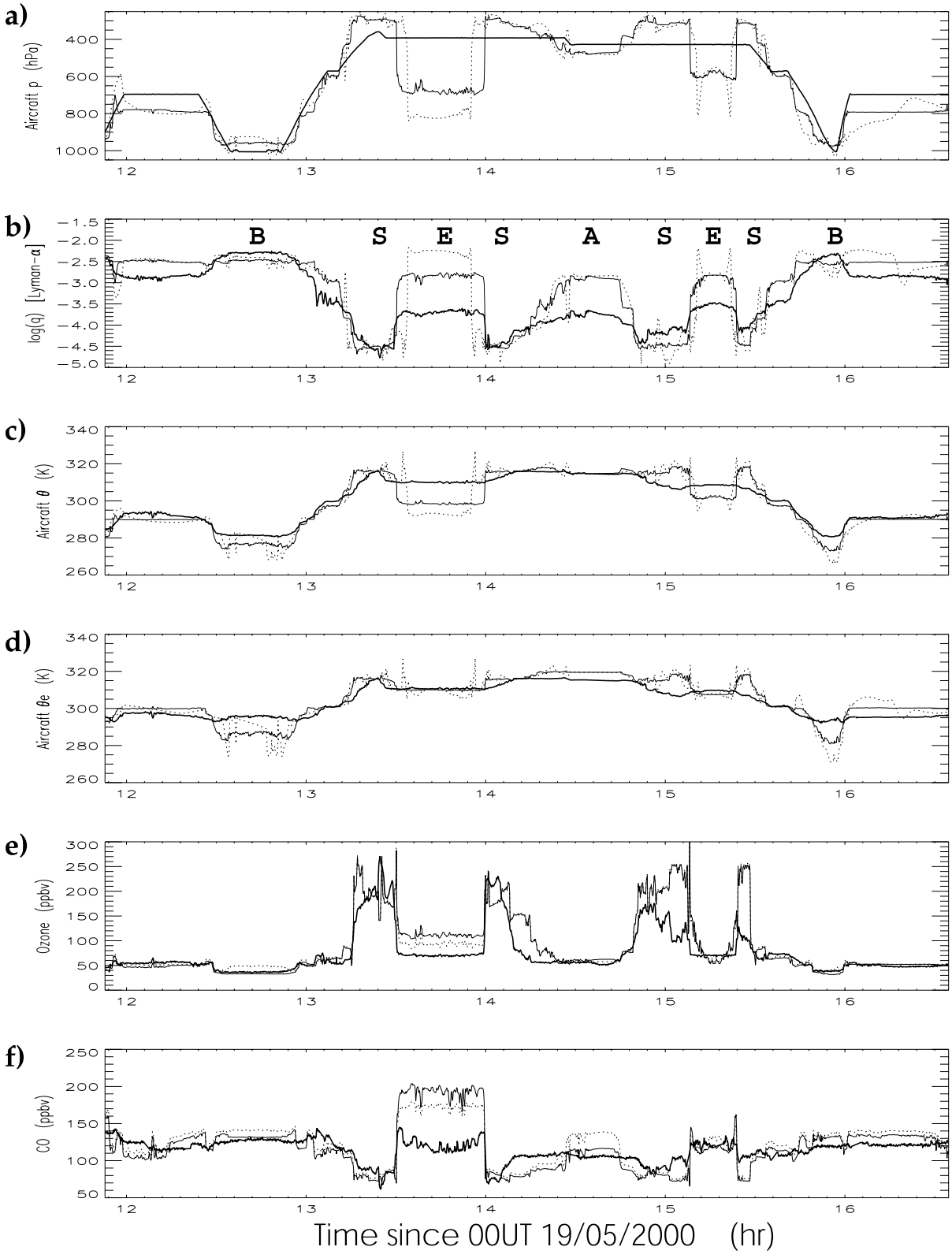

Figure 4. Time series of observations (bold lines) along the ACTO flight on 19 May 2000 compared to results from trajectory simulations. (a–d) Pressure, log(q), θ and θ_e. The dotted lines show the values interpolated from ECMWF analyses to the trajectory origins at 12 UT, 17 May 2000. The solid lines show the air mass average of these modeled values (see section 3.2). (e–f) Ozone and CO concentrations. The dotted line is the air mass average of the values at the origin of trajectories used to initialize the CiTTyCAT chemical model (12 UT, 14 May 2000). The solid line is the air mass average of the final CiTTyCAT results. Their difference indicates chemical change over the last 5 days.

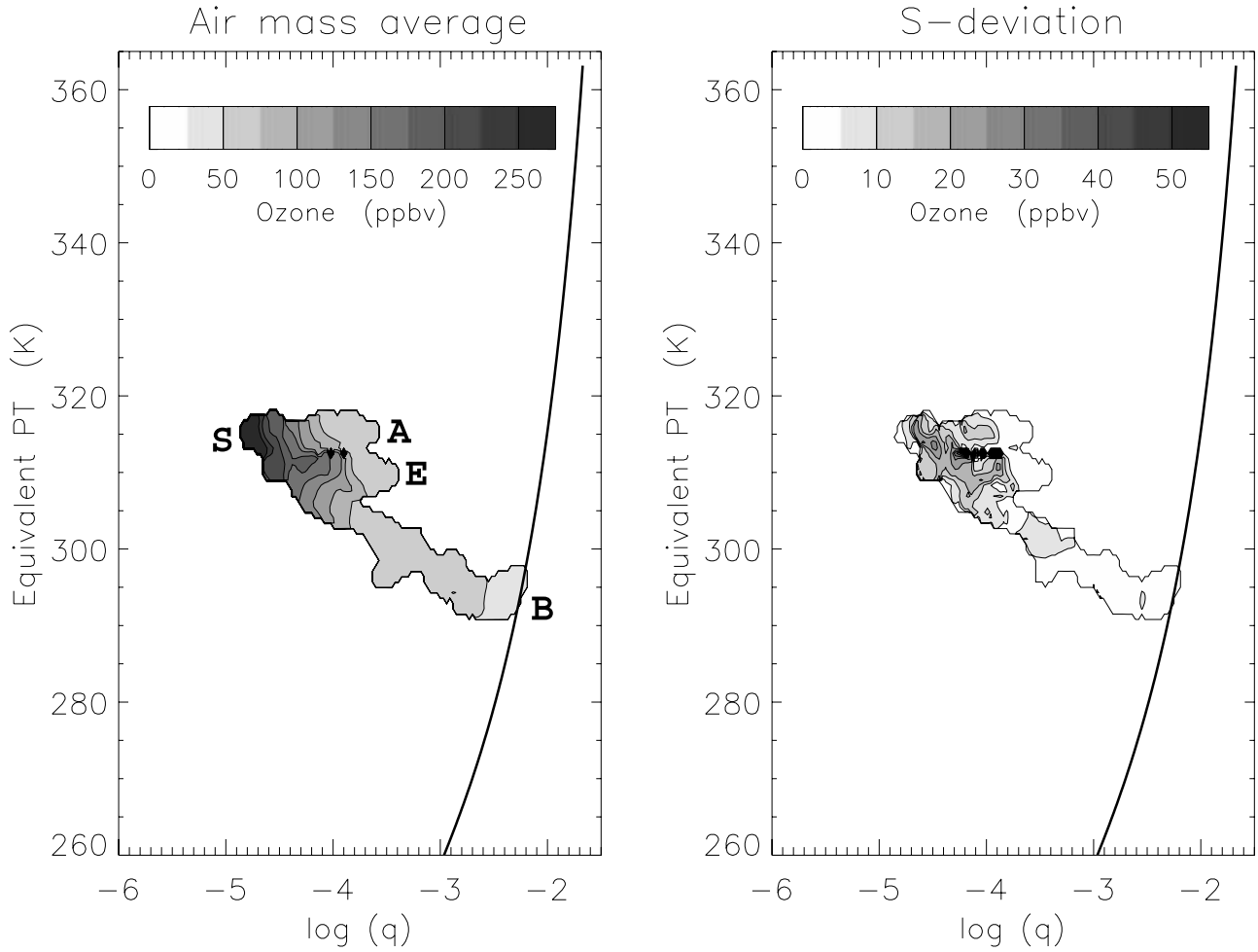

Figure 5. Ozone observations averaged in coordinates defined by the humidity and temperature measured by airborne instruments (I-coordinates). The letters label air masses (see section 3.1). Right: The standard deviation in ozone about the ''air mass average'' is small. Saturated air parcels at 1000 hPa must lie on the curve shown.

$\alpha \log(q)$ and $y = \theta_e$, $\mathbf{x}_i$ is a point along the aircraft flight track at time t_i, and their separation is given by $r = |\mathbf{x} - \mathbf{x}_i|$. The x-axis is scaled by the factor $\alpha = 20$ K so that the kernel is approximately circular in Figure 5, given the range of both axes required to encompass the air mass characteristics. The kernel width $R = 2$ K was chosen objectively by finding a balance between the information lost by averaging observations and the improvement in the correlation with model results that averaging brings (see section 3.3). The kernel is normalized so that:

$$\iint K_i(\mathbf{x})\, dx\, dy = 1. \tag{2}$$

[39] The flight track is divided into n points at 10s intervals and the ''flight density'' in thermodynamic coordinates is defined by:

$$\rho(\mathbf{x}) = \frac{1}{n} \sum_{i=1}^{n} K_i(\mathbf{x}). \tag{3}$$

following the density estimation techniques of *Silverman* [1986] and *Hodges* [1996]. The air mass average of observations c_i is defined as:

$$\bar{c}(\mathbf{x}) = \frac{1}{n\rho(\mathbf{x})} \sum_{i=1}^{n} c_i K_i(\mathbf{x}) \tag{4}$$

with standard deviation $s[c]$ given by the square root of:

$$s^2[c](\mathbf{x}) = \frac{1}{n\rho(\mathbf{x})} \sum_{i=1}^{n} [c_i - \bar{c}(\mathbf{x})]^2 K_i(\mathbf{x}). \tag{5}$$

[40] The standard deviation of ozone in Figure 5 shows the part of the ozone signal that cannot be described by the average relationship between ozone and the thermodynamic properties of an air mass. Note that s is very small for ozone relative to the air mass average concentrations.

3.2. Air-Mass-Averaged Time Series

[41] Most of the variation in the observed concentrations of long-lived chemicals can be explained by the movement of the aircraft between air masses with different thermodynamic signatures. For example, as the aircraft moves around

Figure 5 (as its (q, θ_e) coordinates change) it will pass between air masses with contrasting average ozone values. It is possible to construct an ''air-mass-averaged time series'' of observations (shortened to AO series for Average of Observations) from the values of average ozone as the aircraft moves around the thermodynamic diagram. The rank correlation between the AO (not shown) and unaveraged (bold line in Figure 4e) ozone time series is 0.95.

[42] The technique shares many features in common with ''origin averaging'' described by *Methven et al.* [2001]. In that case a month-long time series of observations, c_i, from a single point (Mace Head, Ireland) was analyzed. The relationship between observed concentrations and the origin of air masses was explored by placing kernels at the origin of each air mass trajectory on a map and weighting those kernels with c_i (as in equation (4)). In general, flight data is described much better in terms of air masses defined by their observed thermodynamic properties, rather than the longitude and latitude at the modeled origin of trajectories.

[43] The chief advantage in constructing air-mass-averaged time series comes when comparing model results with the observations. Similar diagrams to Figure 5 can be constructed using model time series to label the aircraft points, t_i. The air mass average of the model results is then read from the diagram following the aircraft (position $\mathbf{x}_i$), producing an AM time series (Average of Model results). The thin solid line in Figure 4b shows the AM time series for specific humidity. Note how the transitions between air masses now coincide with the observations of q. The rank correlation between model and observations increases from 0.68 to 0.88 under averaging. The effects of trajectory phase errors have been reduced. The most obvious drawback of the averaging procedure is that the high q analyzed at the origin of trajectories in air mass E is averaged with very low values on the flanks of the intrusion, S, because the model intrusion has a displacement error.

[44] Averaging also removes narrow spikes in the observations and model simulations that cannot be explained by movement between air masses. For example, many of the spikes in the simulated θ_e time series (Figure 4d) are averaged out, while retaining an extremely high correspondence with the observations (rank correlation 0.91). In air mass E, the AM θ_e time series (thin solid line) matches the observations to within 2 K.

[45] A stricter test of the method is obtained using chemical concentrations which are independent of the thermodynamic coordinates. In order to do this it is necessary to use the CiTTyCAT Lagrangian model to simulate emissions, photochemistry and deposition along each 3-D trajectory, resulting in its initial and final values of concentration. These time series have been used to construct air mass average diagrams like Figure 5 for initial and final model values. The movement of the aircraft around the diagrams is then used to construct the AM time series of the initial (dotted lines) and final (thin solid lines) concentrations in Figures 4e and 4f.

[46] AM ozone values match the observations closely. The rank correlation squared between model and observations is increased from 0.17 to 0.79 under averaging. The massive correlation increase arises largely because model ozone values are very variable within the stratospheric intrusion, due to the tight ozone gradients near the tropopause, and these spikes are smoothed out by averaging. Furthermore, the transitions between air masses coincide after averaging.

[47] Ozone production is readily apparent only in the polluted European air mass E, showing a net ozone increase of roughly 20 ppbv over 5 days. It appears that model values start too high and move further from the observed values with chemical production, reducing confidence in the model results. However, this is partly an artifact of averaging the high ozone from the flanks of the simulated stratospheric intrusion, S, with air mass E. In section 5 more robust conclusions on ozone production and loss are obtained, taking into account model error.

[48] Model concentrations match the observed ozone well within S on the upper flight leg. Since photochemical ozone changes are very slow within this air mass, the correspondence indicates that trajectories have correctly modeled the origin of the air and that the TOMCAT ozone used for initialization has a reasonable representation of the gradient above the mid-latitude tropopause. On the lower flight leg the observed ozone is much lower than the simulated value. The difference is even more pronounced on the final descent through S (15:28 UT). This is likely to arise from the action of mixing between stratospheric and tropospheric air on the lower, eastern portion of the fold (see Figure 2). CiTTyCAT does not represent mixing and therefore ozone values are not reduced.

[49] The carbon monoxide AM time series corroborates the conclusions drawn from q and ozone. The model matches observations well on the upper flight leg through S, but underestimates concentration at the lower, eastern flank of the fold, suggesting that the fold has experienced mixing with its (higher CO) surroundings. In other air masses the CO correspondence is not as good as for ozone; the correlation squared only increases from 0.22 to 0.54 under averaging. The most striking difference is on the upper leg through air mass E, where CiTTyCAT was initialized with high CO concentrations from the TOMCAT model boundary layer and then picked up more emissions crossing northwest Europe before the final two days uplift to the aircraft location (Figure 3). The model CO concentrations may be much higher than observations because the boundary layer in TOMCAT is too polluted or because considerable mixing between air mass E and its surroundings had reduced CO levels and CiTTyCAT does not represent this process. The high level of primary pollutants in CiTTyCAT following air mass E will tend to result in an overestimate of ozone production rates by the model.

[50] Throughout the flight the correspondence in ozone concentration between model and observations appears remarkably good. However, section 5 addresses just how low model error must be in order to obtain robust conclusions on ozone photochemical production and loss.

3.3. Sensitivity to Averaging Procedure

[51] The comparison of model simulations with observations depends on the degree of smoothing used to define the air mass averages in thermodynamic coordinates. This depends only upon the shape of the averaging kernel. In Figure 6a the solid line shows the correlation (AM-AO) between the averages of modeled and observed ozone as a function of kernel radius, R. Their correlation clearly increases with R as smoothing becomes more severe.

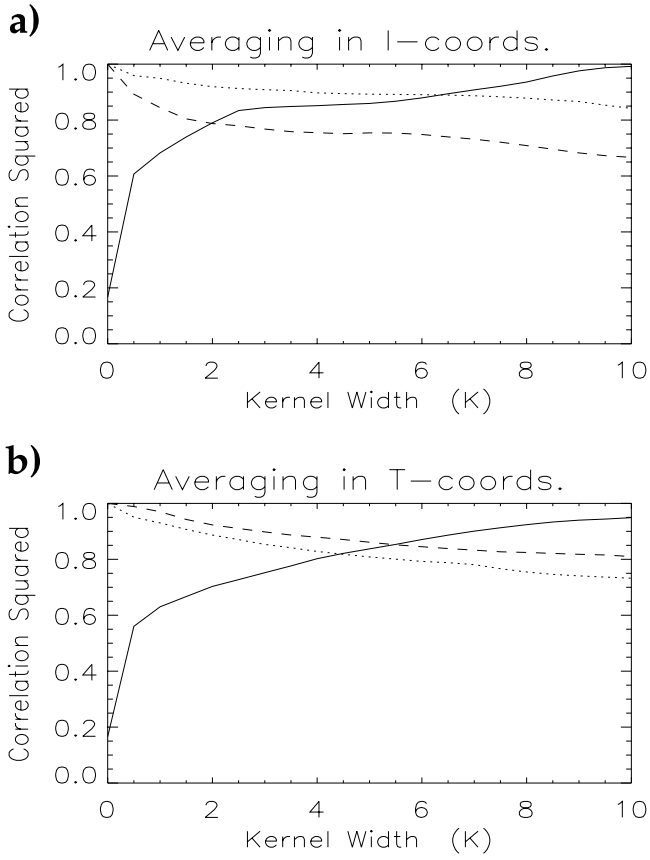

Figure 6. The sensitivity of ozone time series to the kernel width used for air mass averaging. The dotted line shows the rank correlation (squared) between averaged and unaveraged ozone observations (AO-UO). The dashed line shows a similar correlation but for CiTTyCAT model results (AM-UM). The solid line shows the correlation between the averaged modeled and observed time series (AM-AO). (a) Using I-coordinates for averaging (see section 3.3). (b) Using trajectory-based coordinates (section 4.2).

However, as R increases the correlation between the averaged and unaveraged time series obviously falls. For a given kernel width, the observations are less affected by averaging (dotted line) than the model results (dashed line) because of the trajectory phase errors. For example, the aircraft moves into air mass E at a time (13:30 UT) when modeled ozone is still high (or q is low) because the stratospheric intrusion is displaced to the east in the simulation (see Figure 4b). Thus, the flanks of the simulated intrusion are averaged with the simulated values for the polluted air mass E.

[52] Kernel width is chosen to make a significant improvement to the AM-AO correlation, without being too detrimental to the observed or modeled signal. The results are quite insensitive for $2 < R < 6$ K, and the smallest acceptable radius was chosen ($R = 2$ K).

4. Air Mass Transformation

4.1. Physical Evolution Viewed in Thermodynamic Coordinates

[53] In the last section it was shown that chemical variations observed along a flight can be almost entirely described by movement between air masses with different thermodynamic characteristics because they are related to the origin of air masses. Furthermore, the differences between observed specific humidity and potential temperature and the values analyzed at the origins of trajectories are related to modification of those air masses by physical processes including condensation, latent heat release and mixing. The physical transformation of air masses is examined here by following back trajectories for 5 days in thermodynamic coordinates.

[54] Only those trajectories arriving along the flight track between 12:30 and 15:00 UT are shown in Figure 7. During this period the air masses B, E and A were crossed just once, although the stratospheric intrusion, S, was crossed three times (Figure 4b). This provides a clearer distinction between trajectories, colored by time along the flight, t_i.

[55] Point B marks the marine boundary layer where trajectories are approaching from the north, being heated and moistened by turbulent fluxes above the Atlantic Ocean. Note how the trajectories approach the curve of saturation at the ground and then follow it once saturated.

[56] Air masses A and E have origins in the boundary layer and ascend rapidly within a warm conveyor belt (WCB). Warm conveyor belts have been identified with ascending motion ahead of cold fronts within mid-latitude cyclones [e.g., *Browning*, 1990]. The isentropic system-relative flow of a WCB is roughly parallel to the cold front. *Wernli and Davies* [1997] defined WCBs as a coherent ensembles of trajectories ascending in this manner with origins thousands of kilometers to the south where the environment is warm and moist. The concept of the WCB is based on motion following the flow resolved in atmospheric analyses or forecast models. However, moist convection and turbulence is commonplace within these ascending air masses, tending to mix air between the WCB and the region below it. The effect of mixing with the surroundings is to reduce θ_e and q in the WCB as it ascends poleward, whilst remaining saturated. The path followed by A and E in $q - \theta_e$ coordinates (Figure 7b) is not completely straight, as would occur for mixing alone, because condensation is important in reducing q.

[57] Changes in θ_e outside the boundary layer or WCBs are slow, since θ_e is not affected by latent heat release. Radiative cooling to space leads to a slow θ_e decrease in the upper troposphere and stratospheric intrusion (timescales of about 30 days). Mixing also occurs on long timescales, eventually removing contrasts between air masses. Figure 4 presents clear evidence that the lower, narrower parts of the stratospheric intrusion have experienced mixing, tending to reduce ozone but increase q and CO.

[58] Ascending air masses A and E condense out most water vapor as they approach the upper troposphere, but remain much more moist than the stratospheric air, S (see observations in Figure 4b). The range of q spans many orders of magnitude with the result that dry air masses with different origins are not readily distinguished when the q axis is linear (Figure 7b). Since $q - \theta_e$ is also not a true conserved variable diagram we have opted to use $\log(q)$ as the abscissa (Figure 7a) so that dry air masses are well separated.

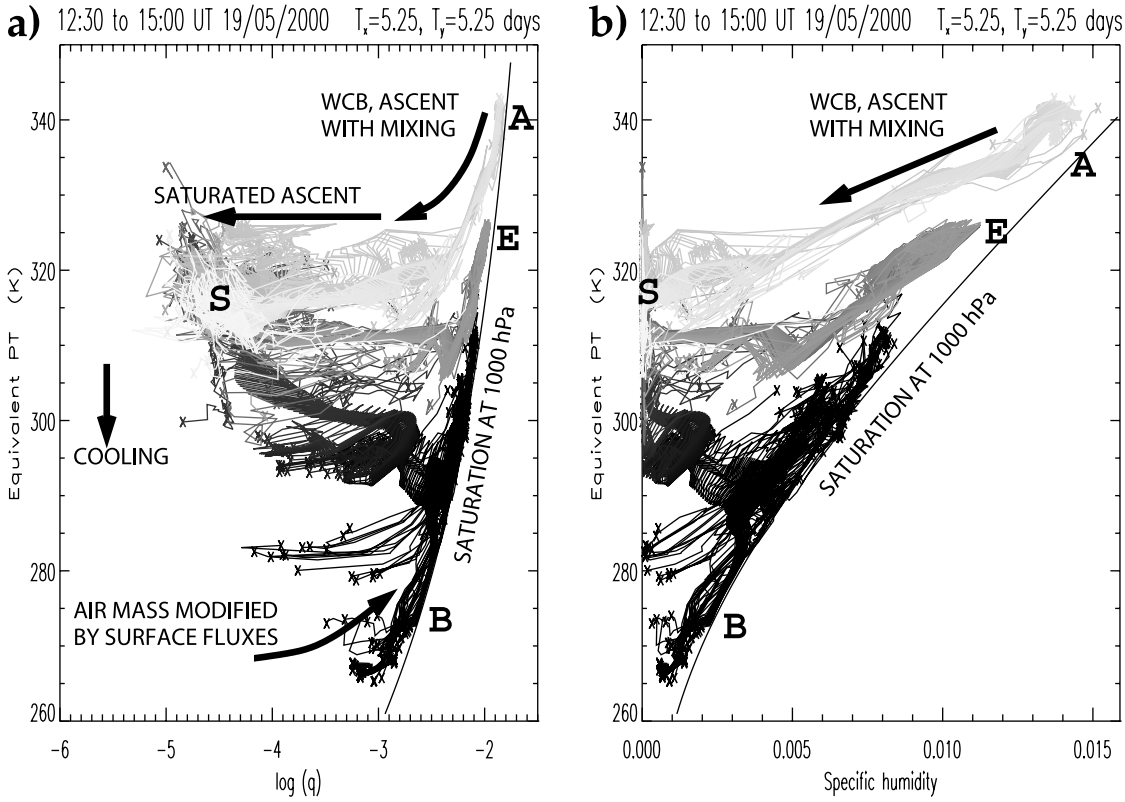

Figure 7. Five day back trajectories arriving along the aircraft flight track at 10s intervals, shown in coordinates given by specific humidity and θ_e interpolated (in time and space) from ECMWF analyses to each trajectory. Using (a) $\log(q)$, or (b) q as the abscissa. The shading denotes the time of arrival along the flight (darkest at 12:30; lightest at 15:00 UT) and the letters label different air mass classes (see text).

[59] Note that some trajectories from air masses A and E appear to move all the way towards stratospheric humidities in Figure 7a. This extra drying (to humidities lower than observed in A and E) is artificial and arises because the spatial resolution of the ECMWF analyses is too low to represent the fine-scale structure. The dry intrusion in the analyses is smeared out over a wider area at the level of the upper flight leg, so that as trajectories approach the flight track the values of q interpolated from the analyses become unrealistically low. This behavior only affects q along the last half a day of the trajectories as they converge. It can be viewed as the result of numerical dissipation in the ECMWF model being much higher than turbulent diffusion in the atmosphere so that mix-down of air masses occurs too early. This behavior highlights the fact that the thermodynamic changes seen along trajectories are dependent upon physical parameterizations in the ECMWF model, its resolution and upon the quality of its data assimilation system. The striking agreement between θ_e at trajectory origins and that observed by an airborne instrument independent of the analysis system (Figure 4d), is an excellent demonstration of the quality of the current ECMWF operational analysis system.

4.2. Classifying Air Masses

[60] As air masses converge on the domain sampled by the aircraft, their thermodynamic characteristics become more similar as a result of the physical processes involved. For example, specific humidity is constrained to low values in the upper troposphere by its saturation vapor pressure. Air masses also mix with each other to some extent as they come into proximity. The trajectories in Figure 7a converge approximately towards the observed distribution of $\log(q)$ and θ_e shown in Figure 5. As a result, air masses are more distinct in thermodynamic coordinates if the simulated values at the origin of trajectories are used to define $(\log(q) - \theta_e)$. As trajectory length increases, flight track points tend to be separated more widely and the averaging kernels used to estimate concentrations overlap less, reducing the smoothing in the air mass averaged time series. However, beyond three days, averaged observations begin to correlate less well with the model simulations because longer trajectories are less reliable and the effects of mixing play a significant role. The results presented here are not sensitive for trajectory lengths between 1.5 and 3 days and T = 2 days is used to define the trajectory-based $q - \theta_e$ throughout the paper (hereafter called T-coordinates, as opposed to I-coordinates defined by $q - \theta_e$ from the airborne instruments).

[61] The contrasting history of air masses is brought out in Figure 8a which shows the T-coordinates average of the change in pressure over 5 day trajectories arriving along the flight track. Ascent is clear for air masses A and E, while elsewhere net descent has occurred.

[62] The observations fall naturally into 7 air mass classes defined using trajectory information alone (i.e., independent

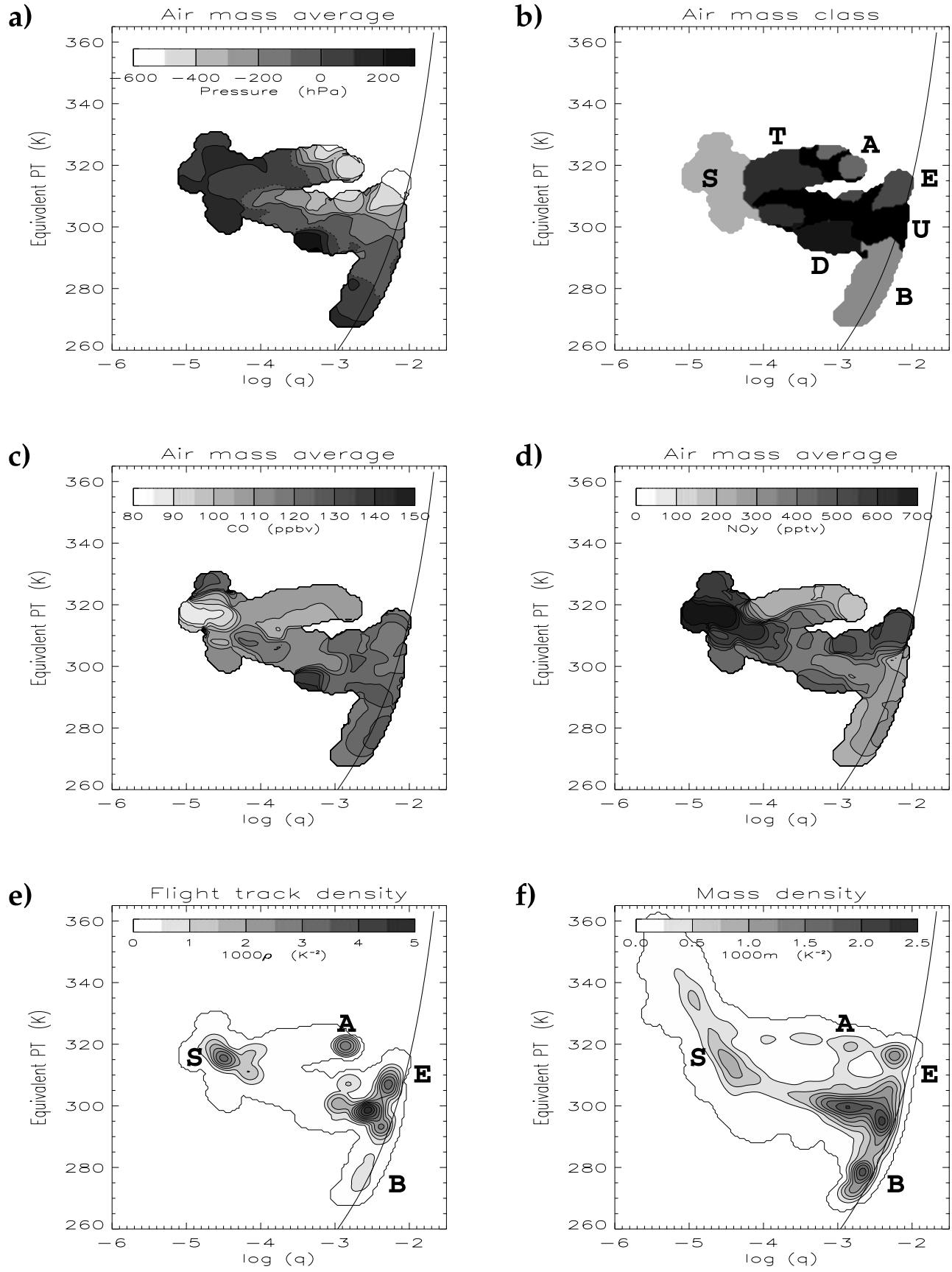
a)
Air mass average
−600 −400 −200 0 200
Pressure (hPa)
b)
Air mass class
T
A
S
E
U
D
B
c)
Air mass average
80 90 100 110 120 130 140 150
CO (ppbv)
d)
Air mass average
0 100 200 300 400 500 600 700
NOy (pptv)
e)
Flight track density
0 1 2 3 4 5
1000ρ (K⁻²)
f)
Mass density
0.0 0.5 1.0 1.5 2.0 2.5
1000m (K⁻²)
Equivalent PT (K)
log (q)

of the chemical observations). The areas labelled A and E in Figure 8b both experienced ascent of more than 400 hPa over the last 5 days and are distinguished by their origin over the American side of the Atlantic (A) or over Europe (E). Air masses S,B,T and D experienced descent or net ascent of less than 80 hPa. Air of stratospheric origin, S, is distinguished by potential vorticity (PV) greater than 2 PVU (1 PVU = 10^{-6} m^2 s^{-1} kg^{-1} K), a common definition of the dynamical tropopause. Air mass T descends along-side the stratospheric intrusion close to the tropopause, whilst D experiences stronger descent from the mid-troposphere towards the BL. The rest of the air mass diagram is unclassified (U).

[63] There is a clear correspondence between the observed chemical concentrations and the air mass classes. Figure 9b shows the observed ozone concentrations averaged in T-coordinates (TAO average). Note how the separation of the air masses is much greater than in the equivalent I-coordinates diagram (IAO average in Figure 5). The stratospheric intrusion, S, is obviously high in ozone and reactive nitrogen (NO_y in Figure 8d) but low in CO (Figure 8c). These correlations are typical of the lower stratosphere [e.g., *Murphy et al.*, 1993; *Fischer et al.*, 2000].

[64] Air mass E carries the signature of recent pollution in NO_y, although it is not as highly polluted in CO as simulated by CiTTyCAT. This may be a result of mixing with air below the warm conveyor belt over a region with low emissions (i.e., the North Sea), as discussed in section 4.1. The ozone is also slightly elevated relative to the marine boundary layer air, B.

[65] Air mass A is very low in NO_y and is only slightly elevated in CO relative to the stratosphere. If pollution was picked up from the USA, then it has aged considerably (reducing NO_y) and been diluted by mixing (reducing long-lived CO). The trajectories (Figure 3) indicate that it has been more than 3 days since air mass A was over the USA. The low NO_y indicates that there has not been very rapid mixing with stratospheric air. However, q and ozone gradients are not as tight between A and S as between E and S (Figure 4). Observed CO in air mass A lies between the simulated values of CO for trajectories from the stratosphere and those ascending from the USA (Figure 4f). All these features implicate mixing on the jetstream side of the tropopause fold as the A and S trajectories travel side by side over the final 1.5 days.

[66] The disadvantage of averaging in T-coordinates, rather than I-coordinates, is that the observations are more affected by averaging. The dotted line in Figure 6b shows the correlation between averaged and unaveraged ozone observations (TAO-UO) versus kernel width, and the dashed line shows the results of averaging the modeled ozone (TAM-UM). Observations are altered more severely by averaging because trajectory phase errors result in the miss-timing of changes in q and θ_e relative to the observed transitions in air mass (see Figure 4b). As a result, observations are to some extent smeared between air masses in T-coordinates. For example, the maximum in TAO ozone (Figure 9b) in air mass S is not as high as in IAO ozone (Figure 5) because the highest ozone occurs in the driest air, but this does not exactly coincide with the lowest modeled q values. As in section 3.3, kernel width is chosen so that averaging is not too detrimental to the observations; a kernel radius, R, of 4 K is used in T-coordinates.

[67] The major advantage of using T-coordinates is that it is possible to estimate the mass occupied by each air mass class. The arrival grid boxes for the RDF3D trajectories are approximately equal in volume. Therefore, the number of RDF3D trajectories with origins characterized by properties in the ranges $q \rightarrow q + \delta q$ and $\theta_e \rightarrow \theta_e + \delta\theta_e$ is proportional to the volume of the arrival domain with these origins. Each level of the arrival grid is a pressure surface, p_l, and the pressure difference, $\Delta p_l = (p_{l-1} - p_{l+1})/2$, is proportional to the mass of a layer. The mass density in T-coordinates (Figure 8f) is estimated by applying equation (3) to the set of RDF3D trajectories, weighting each trajectory by $L\Delta p_l / \Sigma_{l=1}^{L} \Delta p_l$ for its arrival level l.

[68] It is clear that the aircraft did not sample the domain evenly by mass since the flight track density (Figure 8e) is different from the mass density. The aircraft spent most time in the targeted air masses S, A and E. However, in crossing between them the aircraft sampled most of the air masses occupying the domain, except stratospheric air above the unperturbed tropopause which lies on the obvious branch for $\theta_e > 330$ K. The mass density will be used in section 5 to weight the modeled ozone change so that a representative ozone budget can be obtained for the whole domain sampled.

4.3. Chemical Transformation With Estimates of Uncertainty

[69] Chemical reaction, emission and deposition are modeled along trajectories using CiTTyCAT. On average the modeled ozone (Figure 9a) is overestimated in air mass S because mixing had been active at the lower flight leg through the stratospheric intrusion (Figure 4e) and this was not accounted for by the model. The systematic model error as a function of air mass is obtained by averaging the difference between modeled and observed ozone (at each time t_i) in T-coordinates (Figure 9c). At some points in air mass S the model overestimates ozone by almost 200 ppbv. Elsewhere systematic model errors are much smaller and can be positive or negative. The "random" component of model error (Figure 9d) is estimated using the standard deviation of model error in T-coordinates using equation (5). It clearly shows highest values in air masses S and T because simulated ozone values are sensitive to the location of trajectory origins relative to the tropopause where humidity and ozone gradients are extremely large.

Figure 8. (opposite) Diagrams in T-coordinates (see section 4.2 for details) defined by thermodynamic properties at trajectory origins on 12 UT, 17 May 2000 (about 2 days before arrival along flight track). (a) Change in pressure between 12 UT, 14 May 2000, and arrival (about 5 days). Negative values imply net ascent over the trajectories. Zero contour is dotted. (b) Air mass classes defined using trajectory properties. (c) Observed CO concentrations. (d) Observed NO_y concentrations. (e) Density, ρ, of regular points along the flight, x_i. (f) Mass density, m. Both densities are normalized so that their integral (2) is unity.

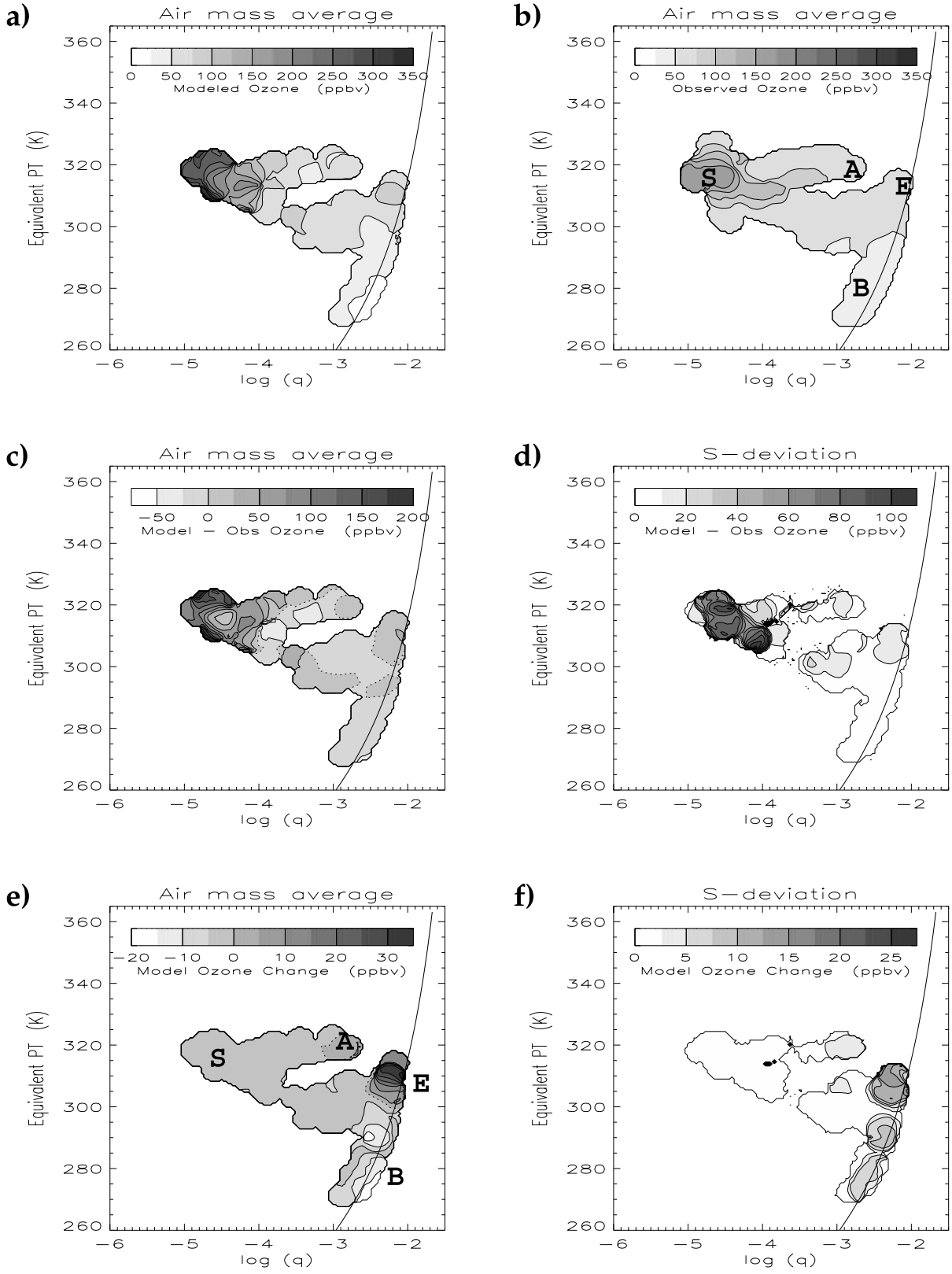

Figure 9. Diagrams in T-coordinates defined by thermodynamic properties at trajectory origins on 12 UT, 17 May 2000 (about 2 days before arrival along flight track). (a) Air mass average of CiTTyCAT model ozone. (b) Average of ozone observations. (c) Air mass average of error (model minus observations). Zero contour is dotted. (d) Standard deviation of model error. (e) Air mass average of ozone change modeled along 5 day trajectories. (f) Standard deviation in modeled ozone change.

[70] Photochemistry acts slowly on ozone and therefore net ozone changes following air masses are small relative to the contrasts in ozone between neighboring air masses. Figure 9e shows the average change in ozone along 5 day trajectories. The CiTTyCAT model indicates ozone production in the polluted air uplifted from the European boundary layer (E) and from the American side of the Atlantic (A). Net loss (mainly deposition) occurs in the marine boundary layer (B). Elsewhere ozone change is slight and negative. The standard deviation in ozone change (Figure 9f) is largest in the uplifted air masses and in the boundary layer. This reflects the variability in the emissions of primary pollutants picked up following trajectories.

5. Mass-Weighted Ozone Budget

[71] Average modeled ozone production within each air mass class is estimated by integrating average ozone change (Figure 9e), weighted by the mass density (Figure 8f), over each of the classes (Figure 8b) in thermodynamic coordinates:

$$\langle \overline{\Delta c} \rangle_J = \frac{1}{M_J} \iint_J \overline{\Delta c}(\mathbf{x})\, m(\mathbf{x})\, dx\, dy \tag{6}$$

where Δc is the final minus initial CiTTyCAT ozone value and M_J is the relative mass occupied by class J, given by the integral of mass density $m(\mathbf{x})$ over the area of the class in T-coordinates. The standard deviation about the class average is given by the square root of:

$$\mathcal{S}_J^2[\Delta c] = \frac{1}{M_J} \iint_J \frac{1}{n\rho(\mathbf{x})} \sum_{i=1}^{n} \left[\Delta c_i - \langle \overline{\Delta c} \rangle_J \right]^2 K_i(\mathbf{x}) \times\ m(\mathbf{x})\, dx\, dy$$

$$= \langle s^2[\Delta c] \rangle_J + \left\langle \left[\overline{\Delta c} - \langle \overline{\Delta c} \rangle_J \right]^2 \right\rangle_J . \tag{7}$$

[72] The first term denotes the integral of the standard deviation diagram (Figure 9f) over class J and the second term is the variance of the "air mass average" (Figure 9e) about the class average. The results are shown by the top (thick) bar for each class in Figure 10. Each bar is centered on the class average (6) with a width given by twice the standard deviation about the class average (7). The model indicates slow average ozone loss in all classes except the uplifted air masses. The spread is largest in the polluted European air (E).

[73] The bottom (thin) bars are centered on the class average of model error (integral of Figure 9c over each class) with a width equal to twice the standard deviation about the class average (given by equation (7) with Δc_i now representing model error for each time t_i). In the stratospheric and tropopause classes ozone is overestimated by the model. This is because the model does not represent the mixing of the tropopause fold with its low ozone surroundings. The spread is large, partly because only the portion of the fold sampled on the lower flight leg appears to have experienced mixing and partly due to the sensitivity of trajectories running close to the strong gradients at the tropopause (giving large values in Figure 9d). In the other classes model bias is much smaller. However, the random error (spread) is sufficiently large that modeled ozone change is only significant in the uplifted European air.

[74] The percentage of domain mass occupied by each class, M_J, is also indicated on Figure 10. Note how the uplifted air involved in ozone production only includes 7.4% of the mass and integrating over all sampled air masses one obtains slight ozone loss. However, the model error is far larger than the average ozone change, largely due to uncertainties in advection and mixing of air arriving in or near the tropopause fold. It is also worth noting that although the aircraft only flew along a 1-D track through a complex 3-D structure, it successfully sampled 83% of the domain mass, assuming that air masses with a similar thermodynamic properties also share similar chemical characteristics. This assumption is least valid for air masses picking up emissions. For instance, some of the American air mass may be polluted, some not.

6. Conclusions

[75] A novel Lagrangian technique has been developed to quantify ozone production and loss in large volumes of the atmosphere, with model uncertainty estimates based on airborne observations. Any Lagrangian technique deliberately partitions transport (i.e., advection by the flow resolved in analyses) from the effects of chemistry and mixing following the flow. This is a major advantage when the photochemical and mix-down timescales are much longer than the stretching and decorrelation timescales for sets of trajectories.

[76] Trajectory calculations are highly accurate in simulating the structure that results as air masses from different origins are brought into proximity. Specific humidity and θ_e, obtained by calculating back trajectories from a flight track and interpolating ECMWF analyses to the origin of those trajectories (in space and time), capture the observed major transitions in air mass. Although the gradients between air masses are not precisely co-located with those in observations, in the ACTO case study the displacement errors were less than 30 km. By calculating back trajectories from a high-resolution 3-D grid ($\Delta x \approx 16$ km; $\Delta z \approx 0.25$ km) and labeling their arrival points with q and θ_e interpolated to their origins from ECMWF analyses, an "RDF3D simulation" of the air mass structure is obtained with the same accuracy as the along-flight simulations. Comparison with the water vapor channel Meteosat image provides independent, although qualitative, confirmation of the accuracy of the method.

[77] As the atmosphere is stirred by large-scale winds, air masses are brought together from origins which have distinct thermodynamic and chemical characteristics. Therefore, both adiabatically conserved thermodynamic properties and long-lived chemical constituents will indicate the origin of air masses and their gradients will be co-located. Here, the complexity of the chemical distributions was reduced by using 2-D thermodynamic coordinates ($q - \theta_e$) to label air masses. The "air mass average" of ozone was obtained by averaging together aircraft observations which occupy nearby points on the thermodynamic diagram. It was shown that almost all the variation in ozone concentrations along a flight can be

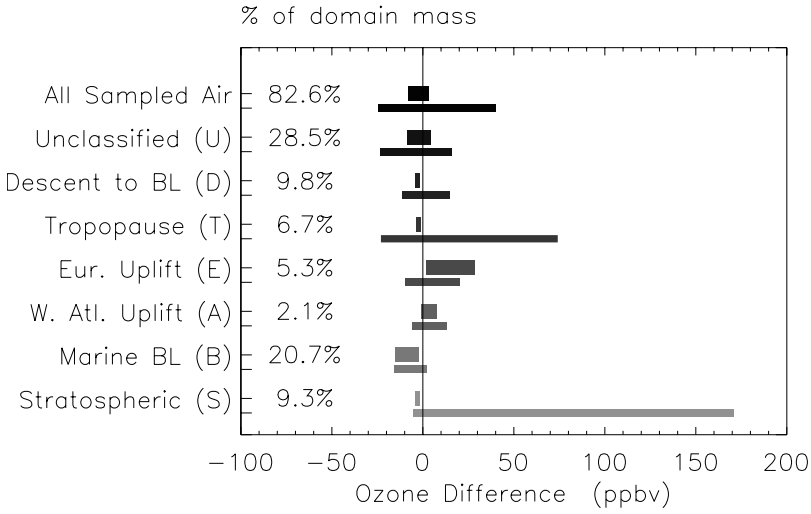

Figure 10. Modeled ozone change (over 5 days) within distinct air mass classes and model error in ozone. The fraction of domain mass (M_J) occupied by each class is given, followed by two horizontal bars. The top, thick bar is centered on the class average of ozone change with a width given by the spread about the class average. The bottom, thin bar shows similar results for model error (derived from model minus observations at each time t_i).

ascribed to the value of air-mass-averaged ozone as the aircraft moves around the diagram.

[78] Similar air mass averages can be calculated by relating modeled concentrations to the observed thermodynamic properties. ''Air-mass-averaged time series'' were constructed to compare the model simulations with observations objectively. For ozone the rank correlation squared between the model and observations was increased from 0.17 to 0.79 by averaging because timing errors in the modeled gradients between air masses are factored out by the averaging procedure. The model is highly capable of modeling the average relationship between the thermodynamic properties of air masses and their chemical composition.

[79] Air masses can also be followed in thermodynamic coordinates by interpolating q and θ_e from atmospheric analyses to every point along back trajectories. Since the θ_e of an air mass is only changed by mixing or external heating and q is also conserved unless water phase changes occur, movement in thermodynamic coordinates indicates physical modification of air masses. Although, the modeled physical changes arise through the parameterizations and data assimilation of the ECMWF analysis system, the correspondence between θ_e observed in warm conveyor belts and the value derived at their origin in the boundary layer many hundreds of km away is remarkable (difference < 2 K). This indicates that the condensation of water vapor and associated latent heat release during large scale ascent (and embedded convection) are parameterized well and moreover that the origin of trajectories is consistent with this. Changes in q and θ_e become unrealistic over the final day of a trajectory because the finite resolution of the ECMWF analyses results in the unrealistically early mix-down of air masses. The RDF3D simulation of air masses represents the opposite limit of no mixing along trajectories. Therefore, trajectory lengths should not exceed the mix-down timescale. For the ACTO case studies a trajectory length between 1.5 and 3 days was found to be optimum.

[80] Subdivision of the atmosphere into air mass classes with distinct transport history (e.g., ascent or descent) is natural in trajectory-based thermodynamic coordinates. Air mass averages of observed chemical concentrations were found to correspond strongly with the air mass classes. Furthermore, modeled chemical change along trajectories and systematic model errors were also naturally partitioned in this way.

[81] The number density of RDF3D trajectory points in $\log(q) - \theta_e$ coordinates was used to estimate the mass density. By integrating mass density over the areas of the diagram covered by the flight track, it was shown that the aircraft sampled air that was representative of 83% of the whole domain mass, if chemical homogeneity within air masses sharing the same thermodynamic characteristics can be assumed. This is the first time that the representativeness of aircraft data has been assessed quantitatively. By calculating mass-weighted integrals over air mass classes, it is possible to estimate the average chemical production/loss that has occurred within each class. Net ozone loss was simulated because only 5% of air was sufficiently polluted for significant ozone production and there was weak ozone loss elsewhere.

[82] Model error can also be estimated for each class and was found to be dominated by the lack of representation of mixing across the tropopause fold by the Lagrangian model and the sensitivity of trajectories originating close to the high gradients at the tropopause. It would be difficult to quantify the integrated effect of mixing experienced by air masses by this method due to its link with transport error. However, clear evidence was presented for mixing on the underside and jetstream side of the tropopause fold.

[83] Elsewhere mixing was sufficiently weak for trajectory simulations, which assume no mixing, to accurately reproduce observations. However, although the Lagrangian model concentration simulations are highly correlated with observations, the photochemistry of ozone is so slow

compared to transport that it is only possible to establish that modeled ozone production is significant in the most polluted air masses in the upper troposphere.

[84] A complementary approach would be to use observations of many more chemicals to calculate instantaneous photochemical ozone production rates. The results could be air mass averaged and compared with the integrated ozone production modeled along trajectories (Figure 9e). If they compared favorably, more confidence could be placed in the modeled production/loss rates than the direct analysis of ozone errors suggests because those errors are dominated by model representation of transport and mixing.

[85] An alternative means to reduce uncertainties in transport and mixing in order to uncover the chemical transformation of air masses would be to conduct a quasi-Lagrangian experiment. One aircraft could sample a polluted air mass, as done here for ACTO, and a second aircraft could intercept the same air mass several days downstream. Photochemistry would have had time to act, the initial composition of the air mass would be well quantified and mixing rates could be inferred from the changes in gradients between air masses, given knowledge of the large-scale strain [*Balluch and Haynes*, 1997]. Transport uncertainties would be dramatically reduced in the results for each air mass class.

[86] In the future the air mass averaging technique will be applied to all flights from the ACTO campaign in order to derive the path-integrated photochemical ozone production or loss within air masses arriving throughout a domain on the Eastern side of the Atlantic with uncertainty estimates. This technique could readily be applied to data from other regions or seasons, whether from campaigns of limited duration or from longer term data sets partitioned by season. However, two-dimensional thermodynamic coordinates do not provide unique markers of air mass origin or history. For instance, in a Northern Hemispheric data set warm, moist air could ascend along a warm conveyor belt embedded within a cyclone over the Atlantic or Pacific. One WCB may ascend from a polluted boundary layer [e.g., *Bethan et al.*, 1998] whilst another may only carry unpolluted marine BL air [e.g., *Grant et al.*, 2000]. It would not generally be possible to distinguish these air masses thermodynamically, they would overlap on the thermodynamic diagram and the inferences about photochemical production would be masked. The manner in which climatologies of air mass properties could best be compiled, so that the budget of ozone can be assessed, is a difficult problem and this technique presents a step towards quantification of the budget constrained by observations.

[87] **Acknowledgments.** The Natural Environment Research Council (NERC) funded John Methven through the ACTO project and continues to fund his research into chemical transport jointly with the Environment Agency through an Advanced Fellowship. NERC funded the ACTO project and flying time as part of the Upper Troposphere-Lower Stratosphere Ozone (UTLS) thematic program. Many thanks to our collaborators in ACTO, especially Kathy Law and Paul Monks for their suggestions for this paper and Stuart Penkett and Claire Reeves for directing the project. Thanks are given to Paul Berrisford, NERC Centre for Global Atmospheric Modelling (CGAM), and John Greenaway, ECMWF, for help with running trajectory forecasts during the field campaign and to Peter Panagi, Joint Centre for Mesoscale Modelling (JCMM), for providing the satellite data.

References

Appenzeller, C., H. Davies, and W. Norton, Fragmentation of stratospheric intrusions, *J. Geophys. Res.*, *101*, 1435–1456, 1996.

Balluch, M., and P. Haynes, Quantification of lower stratospheric mixing processes using aircraft data, *J. Geophys. Res.*, *102*, 23,487–23,504, 1997.

Bethan, S., G. Vaughan, C. Gerbig, A. Volz-Thomas, H. Richer, and D. Tiddeman, Chemical air mass differences near fronts, *J. Geophys. Res.*, *103*, 13,413–13,434, 1998.

Bolton, D., The computation of equivalent potential temperature, *Mon. Weather Rev.*, *108*, 1046–1053, 1980.

Brough, N., NOx and NOy measurements in Maximum Oxidation Rates in the Free Troposphere (MAXOX), in *MAXOX Final Report, ENV4-CT97-0525*, edited by O. Hov, pp. 21–23, Eur. Comm., Brussels, 2000.

Browning, K., Organization of clouds and precipitation in extratropical cyclones, in *Extratropical Cyclones: The Erik Palmen Memorial Volume*, pp. 129–153, Am. Meteorol. Soc., Boston, Mass., 1990.

Cooper, O., et al., Trace gas signatures of the airstreams within North Atlantic cyclones: Case studies from the NARE97 aircraft intensive, *J. Geophys. Res.*, *106*, 5437–5456, 2001.

Edouard, S., B. Legras, and R. Eymard, The effect of small-scale inhomogeneities on ozone depletion in the Arctic, *Nature*, *384*, 444–447, 1996.

Emanuel, K., *Atmospheric Convection*, 580 pp., Oxford Univ. Press, New York, 1994.

Esler, J., D. Tan, P. Haynes, M. Evans, K. Law, P. Plantevin, and J. Pyle, Stratosphere-troposphere exchange: Chemical sensitivity to mixing, *J. Geophys. Res.*, *106*, 4717–4731, 2001.

Esler, J., P. Haynes, K. Law, H. Barjat, K. Dewey, J. Kent, S. Schmitgen, and N. Brough, Transport and mixing between airmasses in cold frontal regions during Dynamics and Chemistry of Frontal Zones, *J. Geophys. Res.*, *108*(D4), 4142, doi:10.1029/2001JD001494, 2003.

Evans, M., et al., Evaluation of a Lagrangian box model using field measurement from EASE 1996, *Atmos. Environ*, *34*, 3843–3863, 2000.

Fischer, H., F. Wienhold, P. Hoor, O. Bujok, C. Schiller, P. Siegmund, M. Ambaum, H. Scheeren, and J. Lelieveld, Tracer correlations in the northern high latitude lowermost stratosphere: Influence of cross-tropopause mass exchange, *Geophys. Res. Lett.*, *27*, 97–100, 2000.

Gerbig, C., S. Schmitgen, D. Kley, A. Volz-Thomas, K. Dewey, and D. Haaks, An improved fast-response vacuum-UV resonance fluorescence CO instrument, *J. Geophys. Res.*, *104*, 1699–1704, 1999.

Grant, W., et al., A case study of transport of tropical marine boundary layer and lower tropospheric air masses to the northern mid-latitude upper troposphere, *J. Geophys. Res.*, *105*, 3757–3769, 2000.

Haynes, P., and J. Anglade, The vertical-scale cascade in atmospheric tracers due to large-scale differential advection, *J. Atmos. Sci.*, *54*, 1121–1136, 1997.

Hodges, K., Spherical nonparametric estimators applied to the UGAMP model integration for AMIP, *Mon. Weather Rev.*, *124*, 2914–2932, 1996.

Inverarity, G., Correcting airborne temperature data for lags introduced by instruments with two-time-constant responses, *J. Atmos. Oceanic Technol.*, *17*, 176–184, 1999.

Law, K., P.-H. Plantevin, D. Shallcross, H. Rogers, J. Pyle, C. Grouhel, V. Thouret, and A. Marenco, Evaluation of modelled ozone using MOZAIC data, *J. Geophys. Res.*, *103*, 25,721–25,741, 1998.

Methven, J., Offline trajectories: Calculation and accuracy, *Tech. Rep. 44*, U. K. Univ. Global Atmos. Model. Programme, Dep. of Meteorol., Univ. of Reading, Reading, UK, 1997.

Methven, J., and B. Hoskins, The advection of high resolution tracers by low resolution winds, *J. Atmos. Sci.*, *56*, 3262–3285, 1999.

Methven, J., P. Berrisford, and B. Hoskins, A Lagrangian climatology for the North Atlantic, *Tech. Rep. 9*, Hadley Cent., Meteorol. Off., Bracknell, UK, 1999.

Methven, J., M. Evans, P. Simmonds, and G. Spain, Estimating relationships between air-mass origin and chemical composition, *J. Geophys. Res.*, *106*, 5005–5019, 2001.

Murphy, D., D. Fahey, M. Proffitt, S. Liu, K. Chan, C. Eubank, S. Kawa, and K. Kelly, Reactive nitrogen and its correlation with ozone in the lower stratosphere and upper troposphere, *J. Geophys. Res.*, *98*, 8751–8773, 1993.

Newell, R., et al., Vertical fine-scale atmospheric structure measured from NASA DC-8 during PEM-West A, *J. Geophys. Res.*, *101*, 1943–1960, 1996.

Ngan, K., and T. Shepherd, A closer look at chaotic advection in the stratosphere. part I: Geometric structure, *J. Atmos. Sci.*, *56*, 4134–4152, 1999.

Nicholls, S., J. Leighton, and R. Barker, A new fast response instrument for measuring total water, *J. Atmos. Oceanic Technol.*, *7*, 706–718, 1990.

Orsolini, Y., P. Simon, and D. Cariole, Filamentation and layering of an idealised tracer by observed winds in the lower stratosphere, *Geophys. Res. Lett.*, *22*, 839–842, 1995.

Parrish, D., J. Holloway, R. Jakoubek, M. Trainer, T. Ryerson, G. Hübler, F. Fehsenfeld, J. Moody, and O. Cooper, Mixing of anthropogenic pollution with stratospheric ozone: A case study from the North Atlantic wintertime troposphere, *J. Geophys. Res.*, *105*, 24,363–24,374, 2000.

Pierrehumbert, R., and H. Yang, Global chaotic mixing on isentropic surfaces, *J. Atmos. Sci.*, *50*, 2462–2480, 1993.

Prather, M., and A. Jaffe, Global impact of the Antarctic ozone hole: Chemical propagation, *J. Geophys. Res.*, *95*, 3473–3492, 1990.

Roelofs, G. J., and J. Lelieveld, Model study of the influence of cross-tropopause ozone transports on tropospheric ozone levels, *Tellus, Ser. B*, *49*, 38–55, 1997.

Silverman, B., *Density Estimation for Statistics and Data Analysis*, Chapman and Hall, New York, 1986.

Stohl, A., and T. Trickl, A textbook example of long-range transport: Simultaneous observation of ozone maxima of stratospheric and North American origin in the free troposphere over Europe, *J. Geophys. Res.*, *104*, 30,445–30,462, 1999.

Tan, D., P. Haynes, A. MacKenzie, and J. Pyle, Effects of fluid-dynamical stirring and mixing on the deactivation of stratospheric chlorine, *J. Geophys. Res.*, *103*, 1585–1605, 1998.

Thuburn, J., and D. Tan, A parameterization of mixdown time for atmospheric chemicals, *J. Geophys. Res.*, *102*, 13,037–13,050, 1997.

Wernli, H., and H. Davies, A Lagrangian based analysis of extratropical cyclones. I: The method and some applications, *Q. J. R. Meteorol. Soc.*, *123*, 467–489, 1997.

Wild, O., K. Law, D. McKenna, B. Bandy, S. Penkett, and J. Pyle, Photochemical trajectory modeling studies of the North Atlantic region during August 1993, *J. Geophys. Res.*, *101*, 29,269–29,288, 1996.

S. R. Arnold, School of the Environment, University of Leeds, Leeds LS2 9JT, UK.

H. Barjat, K. Dewey, and J. Kent, Met Research Flight, Building Y46, Cody Technology Park, Farnborough GU14 0LX, UK.

N. Brough, School of Environmental Sciences, University of East Anglia, Norwich NR4 7TJ, UK.

J. Methven, Department of Meteorology, University of Reading, P. O. Box 243, Earley Gate, Reading RG6 6BB, UK. (j.methven@reading.ac.uk)

F. M. O'Connor, Department of Chemistry, University of Cambridge, Lensfield Road, Cambridge CB2 1EW, UK.

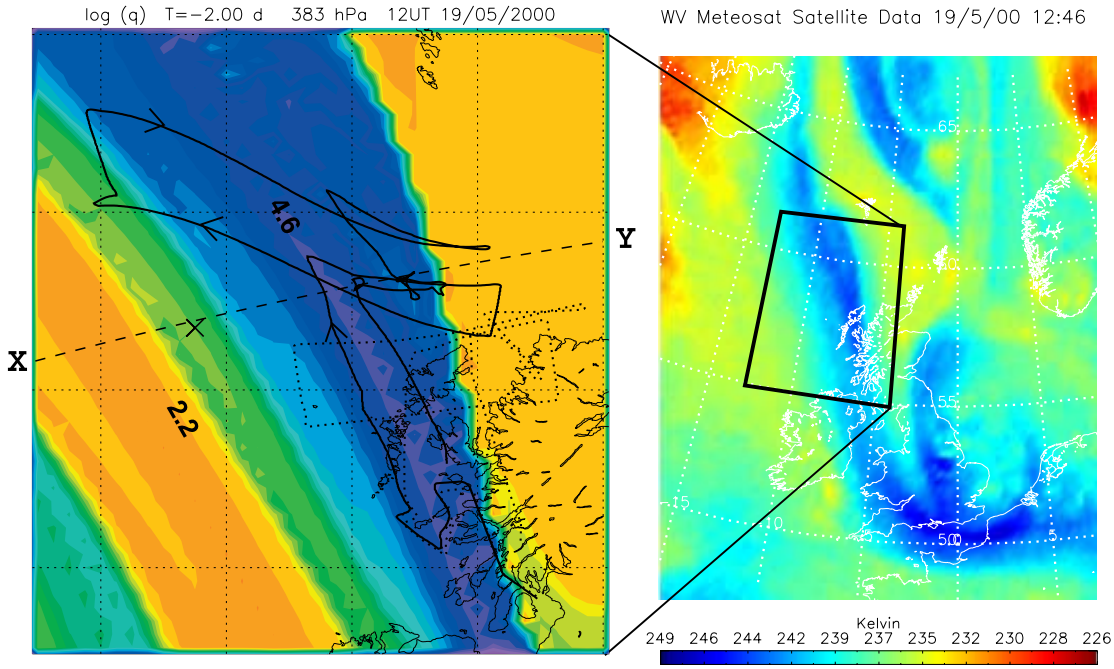

Figure 1. The right panel shows Meteosat water vapor channel brightness temperature at 12:46 UT, 19 May 2000. Blue shading indicates a dry intrusion. The left panel shows a RDF3D simulation of specific humidity at 12 UT, zooming in on the flight domain. Indigo shading is for $\log(q) < -4.6$; orange shading for $\log(q) > -2.2$. The bold dotted line is the aircraft flight track, and the bold solid line is the same track shifted to be relative to the air at 12 UT. The arrows show the direction of flight. The dashed line XY marks the great circle section in Figure 2.

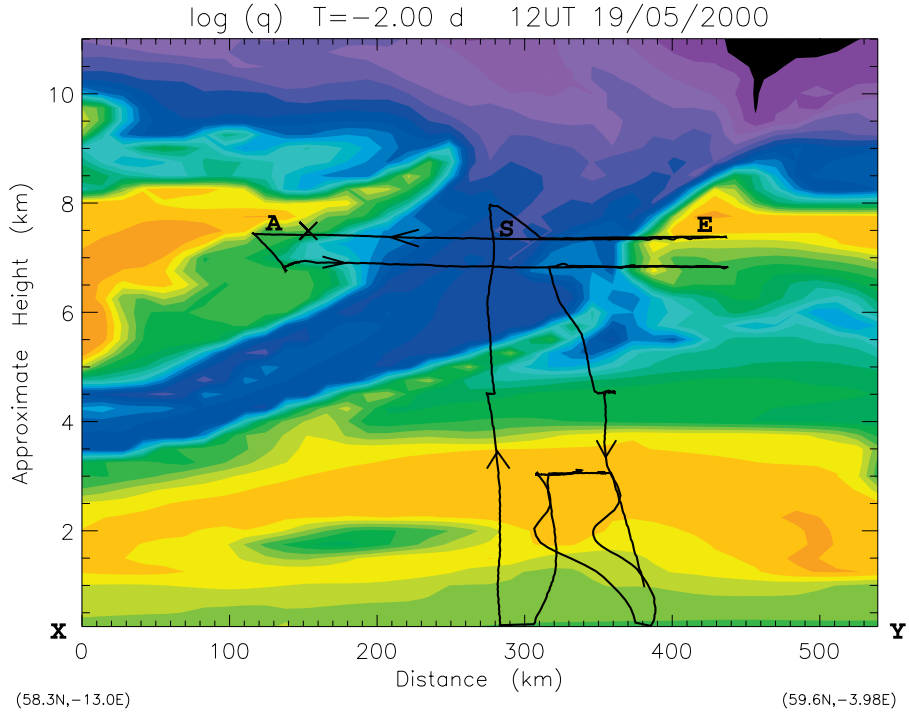

Figure 2. A vertical section across the tropopause fold, seen sloping down to the west. Shading shows specific humidity, as in Figure 1. The solid line shows the projection of the air mass relative flight track onto the section. A, S and E label air masses from the West Atlantic, stratosphere and European boundary layer respectively.